# Lawrence Berkeley National Laboratory

**Title**

Insights into the Enhanced Reversibility of Graphite Anode Upon Fast Charging Through Li Reservoir

**Authors**

Qian, Ji
Zhu, Tianyu
Huang, Di
et al.

Peer reviewed

# Insights into the Enhanced Reversibility of Graphite Anode Upon Fast Charging Through Li Reservoir

Ji Qian, Tianyu Zhu, Di Huang, Gao Liu, Wei Tong*

*Energy Storage and Distributed Resources Division, Lawrence Berkeley National Laboratory, Berkeley, California 94720, United States*
Email: weitong@lbl.gov

## ABSTRACT

Increasing the charging rate and reducing the charging time for Li-ion batteries are crucial to realize the mainstream of electric vehicles. However, it is formidable to avoid the Li plating on graphite anode upon fast charging. Despite the tremendous progress in Li detection techniques, the fundamental mechanism of Li plating and its chemical/electrochemical responses upon cycling still remains elusive. Herein, we present a comprehensive electrochemical method to investigate the fast charging behavior of graphite electrode. A detailed analysis is directed toward understanding the changes in phase, composition, and morphology of the fast-charged graphite. By applying a resting process, we scrutinize the further reactions of the plated Li, which readily transforms into irreversible (dead) Li. We further develop a modified graphite electrode with a thin Ag coating as the Li reservoir. The plated Li can be "absorbed" by the Ag layer to form the Li-Ag solid solution that suppresses the formation of dead Li and provides structural stability, thus promoting the further lithiation of graphite and enhancing the reversibility. This work not only provides new insights into the fast charging behavior of graphite electrode but also demonstrates a potential strategy to improve the fast charging performance of graphite anode.

**KEYWORDS**: Li-ion batteries, fast charging, graphite anode, Li plating, Ag coating

Lithium-ion batteries (LIBs) are the dominant power source for electrical vehicles (EVs).[1] However, recharging EV batteries takes longer than refueling the internal-combustion vehicles. Reducing the charging time is the key to remove the issue of range anxiety about EVs, so as to beat the internal-combustion vehicles and realize the EV mainstream. To achieve this, extreme fast charging (XFC) has been set as a key goal to recharge the battery to 80% state of charge (SOC) under 15 minutes or less.[2, 3]

Fast charging is known to decrease the lifespan and performance of LIBs. During fast charge, Li plating occurs on graphite (Gr) anode, leading to performance decay and raising safety concerns.[4] As a result, it is crucial to characterize the battery degradation behavior and understand the underlying mechanism of Li plating, which is challenging due to the complex and multiscale nature of the degradation mechanism under XFC conditions. Over the past few years, tremendous efforts have been devoted to developing the Li detection and characterization techniques for fast-charged graphite anode.[5-7] These techniques are local or global according to the length scale of detection with regard to the electrode dimension. The global analyses are often performed at the full electrode scale to correlate the degradation process with the overall cell performance.[6] As such, electrochemical techniques, *e.g.*, voltage relaxation,[8, 9] differential voltage,[10] end of charge rest voltage,[11] coulombic efficiency (CE),[12, 13] and impedance spectroscopy,[9] can provide global analyses of the fast charging behavior of graphite anode. However, a comprehensive understanding of the complex reactions between the partially lithiated graphite and plated Li as well as their chemical/electrochemical responses upon cycling still remain elusive.

Here, we develop an electrochemical method, combined with morphological and structural characterizations, to investigate the fast charging behavior of graphite anode. Our study is directed toward investigating the changes in phase, composition and morphology after fast charge of graphite electrode. By applying a resting process after fast charge, we scrutinize the reaction between the partially lithiated graphite and plated Li. We ascertain that the plated Li under XFC conditions readily transforms into dead Li, accounting for the low reversibility of graphite anode. Previous studies show that metals such as Au, Ag, Zn and Mg show definite solubility in Li, and exhibit nearly zero overpotential for Li plating and eliminate Li dendrite formation.[14] In particular, cubic Li-Ag alloys with close lattice constants can form within a wide range of 100-63 in Li at%, which enables an inward growth for Li into the Ag layer rather than deposition on the electrode surface.[15] Accordingly, we demonstrate a modified graphite electrode (Gr-Ag) with a thin Ag layer as the Li reservoir. When the Li plating occurs, the plated Li is "absorbed" by the coated Ag layer *via* reacting with Ag rather than accumulating

on the surface of graphite. Therefore, the Ag-Li solid solution on the surface of graphite electrode serves as a thin buffer layer that stores the solid Li for the further lithiation of graphite and suppresses the dead Li formation. This work not only presents an explicit electrochemical method for early Li detection but also demonstrates a potential strategy to develop improved graphite anode for XFC applications.

## RESULTS AND DISCUSSION

**Fast-Charging Behavior of Graphite Electrode.** To investigate the reversibility of graphite electrode, a testing protocol with (w/) and without (w/o) resting after fast charge are designed (**Figure 1A**). Specifically, the Gr/Li half-cell is charged at 4C to various SOCs (increasing from 10% to 100% progressively) and then slowly discharged to 1.5 V at C/5. Charge/discharge refers to the lithiation/delithiation process of graphite in this work. The slow discharge is designed to achieve the full delithiation of graphite, which is confirmed by measuring the current while holding the cell at 1.5 V after C/5 discharge (**Figure S1**). At each SOC, the cells are cycled twice, with a resting process applied in the former cycle and no resting in the latter cycle. A resting time of 8 hours is selected to ensure the completion of the reaction between the partially lithiated graphite and plated Li (see differential voltage curves, $d$V/$d$t, **Figure S2**) derived from the voltage profiles during resting).

CE at each cycle is presented in **Figure 1B**, showing that the CE starts to decrease with increasing SOC, which becomes more pronounced at SOCs above 20%. The decreased CE could be attributed to the irreversible Li loss due to the Li plating that occurs at 4C charge. When Li plating occurs, the plated Li could be irreversible by reacting with electrolyte and forming dead Li. Alternatively, the plated Li could be reversible *via* Li stripping during discharge and/or further reaction with partially lithiated graphite. The final CE is a result of multiple complex processes including the reversible Li stripping and delithiation of graphite as well as irreversible (dead) Li formation. The lower CE obtained here indicates that the irreversible mechanism is prominent. To gain additional insights into the further reactions, we apply a resting process after fast charge and compare the electrochemical performance to that without a resting process. We first compare the CEs at different SOCs with and without resting, they overlap quite well until 50% SOC, where the difference is noticeable upon further charging to higher SOCs. However, when we examine the ratio of CE with and without resting (*i.e.*, CE$_{w/ resting}$/CE$_{w/o resting}$, donated as φ hereafter), we notice that the φ value first increases till 30% SOC, then decreases at higher SOCs. When there is no Li plating, a resting process results in a negligible impact on CE. The increase in the φ value could be an early indication of Li plating, which will be discussed in detail later. The decreased φ value at higher SOCs

(above 30%) suggests more plated Li, leading to more irreversible (dead) Li on the graphite electrode. For the fast-charged graphite with plated Li, when a resting process is applied, the plated Li reacts with partially lithiated graphite that leads to the loss of electrical contact between graphite and residual Li, thus promoting the formation of dead Li. In contrast, without resting, the dead Li can be partially reactivated and stripped during discharge,[16] although the formation of dead Li during discharge is inevitable.[17-19] We note a similar trend that the φ value decreases with increasing SOC when a resting process is applied in the latter cycle (**Figure S3**). This hypothesis is further verified by the differential discharge capacity curves ($dQ/dV$, **Figure 1C**) derived from the discharge profiles (**Figure S4**). Without resting (solid lines in **Figure 1C**), the delithiation peak for Li metal is observed at a discharge potential below 0.1 V at the SOC higher than 20%, in sharp contrast, there is no delithiation peak associated with Li metal for the cells with resting while the cell voltage goes up above 0.1 V (dash lines in **Figure 1C**), indicating the deposited Li becomes inactive during resting. Correspondingly, when resting is applied after charge, the lithiation degree of graphite electrode slightly increases by comparing the specific capacities of the lithiated graphite at different stages (**Figure S5**) calculated from the $dQ/dV$ plot, confirming the reaction between the plated Li and partially lithiated graphite as described above.

**Prediction of Early Onset for Li Plating on Graphite Anode.** We then use this protocol to study the cells charged at different rates. All the Gr/Li cells show consistent and stable performance during the initial formation cycles (**Figure S6**). CEs and the corresponding φ values at different SOCs and charge rates (C/5, C/2, 1C and 2C) are shown in **Figure S7**. By comparing the φ values (**Figure 2A**), we observe a similar trend. The φ value first remain stable at low SOCs at low to medium rates (up to 1C). At higher rates (≥ 2C), the φ value first increases and then decreases, and a inflection point appears at lower SOC for higher rate. The change in the φ value is attributed to the Li plating on graphite electrode. When the cells are charged at low rates (C/5 and C/2), Li plating does not happen, and the φ value remains stable at ~0.997. The φ value is slightly lower than 1 when the cell is cycled at C/5 with a resting process in the latter cycle (**Figure S8**), suggesting a resting process (*i.e.*, in the former or latter cycle) has no impact on CE at slow charge when no Li plating happens. The φ value lower than 1 is presumably due to the side reactions between the lithiated graphite and electrolyte during resting.[20, 21]

However, when Li plating occurs, the resting process makes differences. Schematic in **Figure 2B** illustrates the charge-discharge processes for graphite with and without resting (resting in the former cycle is presented). Note that the charge capacity is identical for both

cycles, *i.e.*, $Q_{1-charge} = Q_{2-charge}$, so the φ value essentially represents the ratio of $Q_{1-discharge}$ to $Q_{2-discharge}$ (φ = $Q_{1-discharge}/Q_{2-discharge}$). As reported, Li plating during fast charge leads to a cumulative capacity loss for graphite electrode upon cycling.[8] Therefore, when Li plating begins to take place, $Q_{2-discharge}$ becomes lower than $Q_{1-discharge}$, and φ value increases. However, with more Li plating at high SOCs, more irreversible Li forms during resting, and $Q_{1-discharge}$ becomes lower than $Q_{2-discharge}$, leading to a decreased φ value. As such, the change of φ value provides useful information on the onset of Li plating at different rates and SOCs. As shown in **Figure 2C**, no Li plating occurs at C/5 and C/2, and Li plating happens around the SOC of 80%, 40% and 20% at the rate of 1C, 2C and 4C, respectively. This estimation is consistent with the change in CE (red lines in **Figure S7**) and the delithiation peak of Li metal in the *d*Q/*d*V curves (**Figure S9**). With this protocol, the change of φ value provides further information on the relative amount of the plated Li and formation of dead Li. It is worth noting that the estimated SOC for the onset of Li plating at different rates is based on the testing protocol with 10% SOC interval and it may vary with the fabrication of graphite electrode and use of electrolyte.

The phase transformation for graphite at various SOCs are further studied by wide-angle X-ray scattering (WAXS) technique (**Figure S10**). As shown in **Figure S10A**, upon fast charging at 2C and 4C, it can be clearly seen that Li metal is deposited on the graphite electrode, indicating the formation of dead Li even after C/5 discharge. The WAXS studies show that the amount of $LiC_6$ decreases with rate (**Figure S10B**). Moreover, Li metal is detected at a rate higher than 1C (**Figure S10C**). At discharged state (**Figure S10D, E**), all peaks of $LiC_x$ (*e.g.*, $LiC_6$, $LiC_{12}$, $LiC_{18}$) disappear and the lithiated graphite fully reverts back to graphite, however, Li metal is still observed on the fast-charged electrodes (2C & 4C). These results confirm that the plated Li at high rates transforms into dead Li.[22]

**Ag Coating to Improve Reversibility of Graphite Anode.** With the protocol for early detection of Li plating on graphite, we aim to improve the reversibility of graphite under XFC conditions. Here, we introduce a nano-coating layer of Ag that can store the plated Li and thus prevent its accumulation on the surface of graphite electrode as the solid Li during the lithiation of graphite. Ag is coated on graphite electrode by thermal deposition (**Figure S11**) and its thickness is estimated to be ~100 nm based on the deposition rate and time. The deposition of Ag is confirmed by X-ray powder diffraction (XRD) and energy-dispersive X-ray spectroscopy (EDS) mapping (**Figure 3A, B**). With the thin Ag layer, the surface morphology of the modified graphite electrode (Gr-Ag) resembles that of pristine electrode (**Figure 3B** & **Figure S12, 13**).

To understand the effect of Ag layer on the reversibility of graphite electrode, we first investigate the morphology of the graphite and Gr-Ag electrodes after 4C fast charge to 100% SOC. We observe the remarkably different morphologies on the surface of both electrodes. The fast-charged graphite electrode surface is featured by a layer of Li deposition with cracks, and a large amount of Li whiskers are revealed by scanning electron microscopy (SEM) (**Figure 3C**). As shown in the cross-section SEM image (**Figure 3D**), the thickness of the Li layer on the fast-charged graphite is ~9 μm. This thick layer of deposited Li can easily transform into dead Li, causing severe performance decay during cycling.[23] In sharp contrast, no obvious Li dendrite is observed on the surface of the fast-charged Gr-Ag electrode (**Figure 3E, F**), instead, the surface is smooth with no obvious cracking. The presence of Ag on the Gr-Ag electrode surface after charging is confirmed by EDS (**Figure S14**). This study indicates that the coated Ag layer modifies the Li deposition behavior on graphite electrode.

The charge profiles of the graphite and Gr-Ag electrodes are shown in **Figure 3G**, which fully overlap during the initial charge, when only graphite lithiation occurs, suggesting that the Ag coating has a negligible effect on the kinetics of graphite lithiation. However, upon further charging, Li plating occurs and the Ag layer comes into play. For graphite electrode, the Li dendrites grow quickly at a high deposition rate (~12 mA cm$^{-2}$), and break the mechanically unstable solid electrolyte interface (SEI) (**Figure 3C, D**), which leads to the fracture and thus increased overpotential.[24] The subsequent decrease in overpotential can be attributed to the increased pressure. The Li deposition leads to the volume expansion of the Gr electrode and increased pressure, which makes the deposited Li dense and compact.[25, 26] In contrast, the Gr-Ag electrode exhibits a smaller overpotential at a maximum of 256 mV, compared to 386 mV for Gr anode. The Ag coating homogenizes the current distribution, it also shows a solubility for Li, while C does not, therefore, Li nucleation occurs at a lower overpotential in Ag than C.[14] Moreover, the lithiation-delithiation process for Ag is a solid-solution reaction. According to the Li-Ag phase diagram, a solid solution with a cubic structure ($\gamma_1$, $\gamma_2$, and $\gamma_3$ phases) can form in a wide range, 92 – 63.5 in Li at%.[15, 27] The formation of these Li-Ag solid solutions covers an even wider range of Li in wt% (8 to almost 100). Moreover, the $\gamma_1$, $\gamma_2$, and $\gamma_3$ phases have close lattice constants of 0.980, 0.968, and 0.949 nm, respectively. We also run a calculation to understand if the plated Li can be accommodated by the coated Ag. The extreme case of 4C charge (**Figure 3G**) is selected as it represents the maximal Li plating in this study. The areal capacity of the graphite electrode is ~3 mAh cm$^{-2}$. Assuming Li plating occurs at the voltage below 0 V, the capacity below 0 V is ~ 2.7 mAh cm$^{-2}$ (90% total capacity of graphite electrode). The calculated weight of the plated Li is $2.59 \times 10^{-4}$ g cm$^-$

. The amount of the plated Li in the as-formed Li-Ag layer is ~71.2% (Ag amount is $1.05 \times 10^{-4}$ g/cm$^{-2}$), which falls in the range of the Li-Ag solution. Therefore, the freshly formed Li can be accommodated by the Ag layer rather than deposit on the surface of the graphite electrode as the solid Li metal.[15, 28]

The function of Ag-Li reservoir is confirmed by XRD collected on the fast-charged electrodes. For the fast-charged graphite anode (**Figure 3H**), after resting, the ratio of the LiC$_6$ peak intensity to that of LiC$_{12-18}$ increases, indicating a higher lithiation degree of graphite with resting, owing to the reaction between the plated Li and partially lithiated graphite, although there is still some residual Li metal on the electrode with resting (**Figure S15**). In comparison, for the fast-charged Gr-Ag electrode with resting (**Figure 3I**), the lithiation degree of graphite anode is greatly enhanced, and only a minimal amount of LiC$_{12-18}$ is revealed after resting. Moreover, the peak of Li-rich Li-Ag alloy disappears after resting due to its reaction with partially lithiated graphite, leading to the formation of LiAg phase (**Figure S15**).[29, 30] Note that the Li in the LiAg phase is reversible with a dealloying voltage of $0.2 - 0.4$ V,[30] which overlaps with the delithiation of the Gr electrode (stages 2 and 3&4). However, the capacity of the LiAg phase (0.026 Ah cm$^{-2}$ for 100 nm Ag) in this study is negligible compared to that of graphite electrode (3 mAh cm$^{-2}$). The combined XRD and SEM results suggest that the coated Ag acts as the Li reservoir to store the solid Li and mitigates Li deposition and dead Li formation, therefore, improving the reversibility of graphite electrode under XFC conditions.

Given the enhanced reversibility of Gr-Ag electrode, we further investigate its fast charging behavior with the testing protocol presented in **Figure 1A**. CE of Gr-Ag electrode (**Figure 4A**) is higher at each SOC compared to that of unmodified graphite (**Figure 1B**), indicating that the loss of Li is partially alleviated by the Ag coating. This is consistent with the larger delithiation peak of Li-Ag alloy at high SOCs during discharge without resting in the $d$Q/$d$V plots (solid lines in **Figure 4B**) derived from the discharge profiles (**Figure S16**). Meanwhile, the φ value of Gr-Ag electrode increases compared to the unmodified graphite electrode. The increased φ value is attributed to the formation of Ag-Li solid solution that stores the Li and mitigates the Li deposition and dead Li formation.

To compare the fast charging behaviors of graphite and Gr-Ag electrode, we calculate the percentage of discharge capacity from different phases, *i.e.*, Li metal, LiC$_6$ (stage 1), LiC$_{12-18}$ (stage 2), and LiC$_{27-72}$ (stage 3&4) (**Figure 4C, D**) by integrating the corresponding regions in the $d$Q/$d$V plot. The difference in the discharge capacity of LiC$_6$, LiC$_{12-18}$, LiC$_{27-72}$ between graphite and Gr-Ag electrodes is small at low SOCs. With increasing SOC, more discharge capacity from Li metal and Li-Ag alloy in graphite and Gr-Ag electrode, respectively, is

observed. By caulating the difference in normalized discharge capacity with resting and without resting ($Q_{w/ resting}$ - $Q_{w/o resting}$) (**Figure 4E, F**), we find that Li is consumed and converts to $LiC_6$ (stage 1) at high SOCs for Gr-Ag electrode than unmodified graphite during resting. This is an evidence of the improved reversibility for Gr-Ag electrode upon fast charging.

To further verify the improved reversibility of Gr-Ag anode, we perform the cycling tests on graphite and Gr-Ag electrodes in Li half-cells. The cells are charged to 100% SOC at 2C and 4C and then discharged at C/5 (**Figure 5**). At 2C, Gr-Ag and graphite electrodes show similar CEs during the first few cycles. After that, Gr-Ag electrode starts to exhibit a higher CE than unmodified graphite, and the difference becomes even more pronounced upon further cycling. A sudden drop in the CE for graphite occurs at the 26th cycle due to the accumulated dead Li on graphite electrode, while a similar cell failure is postponed to the 43th cycle for Gr-Ag electrode. The sudden drop in CE is mainly due to the exhausted electrolyte. At 2C rate (~6 mA/cm$^{-2}$), the growth of Li whiskers is severe, which rapidly consume electrolyte,[20] especially in the half cells with a Li metal counter electrode. At a high rate of 4C, the difference in CE of graphite and Gr-Ag electrodes can be observed even during the initial cycles because of more severe Li deposition and dead Li formation on graphite, consistent with the differed morphologies of the fast-charged graphite and Gr-Ag electrodes (**Figure 3**). Upon cycling, Gr-Ag electrode shows consistently high CE compared to graphite electrode. In contrast to the sudden drop in CE for graphite at the 21st cycle, no sudden drop is observed for Gr-Ag electrode until the 30th cycle. The preliminary cycling results confirm that the modified Gr-Ag electrode indeed facilitates better reversibility of graphite and Ag coating extends the cycle life of graphite electrode under XFC conditions.

In this work, only Ag coating of ~100 nm is investigated for the proof of concept. We note that the optimization of Ag coating would warrant further improvement in the fast charging performance of graphite electrode. For example, there should be an optimal thickness (amount) of Ag for a given graphite electrode with varied properties (*i.e.*, physical properties of graphite, electrode thickness and formulation *etc.*). Moreover, the optimal Ag amount is strongly correlated with the fast charging condition, which ultimately determines the amount of plated Li to be accommodated by the coated Ag. Compared to many other coating methods, the modification of graphite electrode by coating Ag directly on the electrode surface is facile and effective, given the nature of its functionality. In many circumstances, coating serves to protect the active materials from the undesirable side reactions with electrolyte during electrochemical cycling, therefore, coating is typically favored at the particle level for most active materials. However, for fast charging application, Li plating occurs with the initial

nucleation on the surface of graphite electrode followed by further growth to accumulated Li plating.[31] Therefore, it is not necessary to coat graphite particles for XFC applications, which eliminates the complexity in fabricating uniformly coated particles but a facile process for electrode modification. Based on the functioning mechanism discussed above, Mg is an alternative choice of cost-effective metals to coat graphite electrode for XFC applications given the wide solubility range of Mg for Li.[32, 33]

**CONCLUSION**

We develop a comprehensive electrochemical method to study the fast charging behavior of graphite electrode. Applying a resting process after fast charge allows us to elucidate the complex reactions that involve plated Li, partially lithiated graphite, and irreversible (dead) Li. We find that the plated Li readily transforms into dead Li during resting, leading to severe Li loss and performance decay. The onset of early Li plating for graphite electrode can be predicted based on the $\varphi$ ($CE_{w/\,resting}/CE_{w/o\,resting}$) value, indicating no Li plating, trace Li plating, and more Li plating when it remains stable, increases, and decreases, respectively. This method can be used for any graphite electrode cycled under different conditions. To improve the reversibility of graphite electrode under XFC conditions, we develop a modified graphite electrode with a thin Ag coating as the Li reservoir. This Ag layer modifies the Li deposition behavior on graphite electrode by forming the Ag-Li solid solution that diminishes the Li loss and suppresses the dead Li formation. At high charge rate, the Gr-Ag/Li cell exhibits a higher CE upon cycling than unmodified Gr/Li cell, and Ag coating extends the cycle life of graphite electrode under XFC conditions. This work demonstrates the feasibility to improve the reversibility of graphite under XFC conditions *via* a simple electrode surface coating method. We believe that the fast-charging performance of graphite can be further improved *via* the optimization of the coating layer along with other cell components.

**METHODS**

**Materials.** Pristine graphite electrode used in this study contains 91.83 wt% Superior Graphite SLC 1506T, 2 wt% Timcal C45 carbon, 6 wt% Kureha 9300 PVDF binder, and 0.17 wt% oxalic acid. The areal capacity is ~3 mAh cm$^{-2}$. The Gr-Ag electrode is prepared by depositing thin film of silver on graphite electrode through thermal deposition method using the MBRAUN thermal evaporator at the Molecular Foundry, Lawrence Berkeley National Lab (LBNL). High purity (99.99%) Ag pellet with a size of 1/4" in diameter and 1/4" in thickness is purchased from Kurt J. Lesker Company and used as received. The Ag pellet is placed inside a shielded tungsten boat and the evaporation is conducted at 1100 °C. The deposition process

is performed inside a vacuum chamber under a pressure of $10^{-4}$ Pa with a deposition rate of 1 Å $s^{-1}$.

**Electrochemical Measurements.** All electrodes are dried under vacuum at 120 °C for 12 hours, and then punched into the discs with a diameter of ~12 mm and stored inside a glovebox filled with Ar. The lithium foil (Alfa Aesar) is punched into the discs with a diameter of ~16 mm. The separator (Celgard 2400) with a diameter of ~19 mm is used. 1.2 M lithium hexafluorophosphate (LiPF$_6$) in a mixture of ethylene carbonate (EC) and ethyl methyl carbonate (EMC) with a mass ratio of 3: 7 is used as an electrolyte. All salt and solvents are purchased from Gotion. The Gr/Li half-cells (CR2032) are assembled and tested at 30 °C. The cells are cycled at C/10 (1C = 330 mAh $g^{-1}$) for 10 times between 1.5 and 0.01 as the formation step. The cells are then charged at designated rates (C/5 – 4C) and SOCs (10% – 100%). The charge time is calculated based on the intercalation capacity of the cell on the $10^{th}$ formation cycle to ensure the accurate SOCs. All cells are discharged at C/5.

**Material Characterization.** Cells are disassembled inside an Ar-filled glove box at designated states of charge. Graphite electrodes are washed with dimethyl carbonate (DMC) for three times and then dried inside the glove box. The morphologies are studied using field-emission SEM (JOEL-7500F) with an X-ray detector for EDS mapping. To avoid damage to the electrode, we cut a small slit at the edge of the electrode and then tear it apart. XRD patterns are collected on a Bruker D2-Phaser with Cu Kα radiation (λ = 1.54178 Å). WAXS measurements are performed with an energy of 10 keV and 1% energy bandwidth deltaE/E from a multilayer at beamLine 7.3.3, Advanced Light Source (ALS), LBNL. The scattering intensity is recorded on a 2D Pilatus 2M detector (Dectris) with a pixel size of 172 microns and positioned about 28 cm downstream of the sample. A standard silver behenate sample is measured to calibrate the beam position and sample-detector distance using the Igor Pro Nika package.[34] The samples are kept under helium gas environment (1 atm) to reduce background scattering and attenuation.

## ACKNOWLEDGEMENTS

**Supporting Information**

Electrochemistry of Gr/Li cells cycled at various rates to different SOCs, WAXS patterns of graphite charged to 100% SOC at different rates, SEM images and EDS mapping of graphite and Gr-Ag electrodes at different states, discharge profiles and XRD patterns of fast-charged Gr-Ag anode.

# REFERENCES

1. Li, M.; Lu, J.; Chen, Z.; Amine, K., 30 Years of Lithium-Ion Batteries. *Adv. Mater.* **2018,** *30*, 1800561.
2. Ahmed, S.; Bloom, I.; Jansen, A. N.; Tanim, T.; Dufek, E. J.; Pesaran, A.; Burnham, A.; Carlson, R. B.; Dias, F.; Hardy, K.; Keyser, M.; Kreuzer, C.; Markel, A.; Meintz, A.; Michelbacher, C.; Mohanpurkar, M.; Nelson, P. A.; Robertson, D. C.; Scoffield, D.; Shirk, M. *et al.* Enabling Fast Charging – A Battery Technology Gap Assessment. *J. Power Sources* **2017,** *367*, 250-262.
3. Liu, Y.; Zhu, Y.; Cui, Y., Challenges and Opportunities Towards Fast-Charging Battery Materials. *Nat. Energy* **2019,** *4*, 540-550.
4. Tomaszewska, A.; Chu, Z.; Feng, X.; O'Kane, S.; Liu, X.; Chen, J.; Ji, C.; Endler, E.; Li, R.; Liu, L.; Li, Y.; Zheng, S.; Vetterlein, S.; Gao, M.; Du, J.; Parkes, M.; Ouyang, M.; Marinescu, M.; Offer, G.; Wu, B., Lithium-Ion Battery Fast Charging: A Review. *eTransportation* **2019,** *1*, 100011.
5. Viswanathan, U.; Garrick, T. R.; Fortier, M. E., Review – Lithium Plating Detection Methods in Lithium-Ion Batteries. *J. Electrochem. Soci.* **2020,** *167*, 160552.
6. Paul, P. P.; McShane, E. J.; Colclasure, A. M.; Balsara, N.; Brown, D. E.; Cao, C.; Chen, B. R.; Chinnam, P. R.; Cui, Y.; Dufek, E. J.; Finegan, D. P.; Gillard, S.; Huang, W.; Konz, Z. M.; Kostecki, R.; Liu, F.; Lubner, S.; Prasher, R.; Preefer, M. B.; Qian, J. *et al.* A Review of Existing and Emerging Methods for Lithium Detection and Characterization in Li-Ion and Li-Metal Batteries. *Adv. Energy Mater.* **2021,** *11*, 2100372.
7. Lin, X.; Khosravinia, K.; Hu, X.; Li, J.; Lu, W., Lithium Plating Mechanism, Detection, and Mitigation in Lithium-Ion Batteries. *Prog. Energy Combus. Sci.* **2021,** *87*, 100953.
8. Konz, Z. M.; McShane, E. J.; McCloskey, B. D., Detecting the Onset of Lithium Plating and Monitoring Fast Charging Performance with Voltage Relaxation. *ACS Energy Lett.* **2020,** *5*, 1750-1757.
9. Schindler, S.; Bauer, M.; Petzl, M.; Danzer, M. A., Voltage Relaxation and Impedance Spectroscopy as *In-Operando* Methods for the Detection of Lithium Plating on Graphitic Anodes in Commercial Lithium-Ion Cells. *J. Power Sources* **2016,** *304*, 170-180.
10. Petzl, M.; Danzer, M. A., Nondestructive Detection, Characterization, and Quantification of Lithium Plating in Commercial Lithium-Ion Batteries. *J. Power Sources* **2014,** *254*, 80-87.
11. Tanim, T. R.; Paul, P. P.; Thampy, V.; Cao, C.; Steinrück, H.-G.; Nelson Weker, J.; Toney, M. F.; Dufek, E. J.; Evans, M. C.; Jansen, A. N.; Polzin, B. J.; Dunlop, A. R.; Trask, S. E., Heterogeneous Behavior of Lithium Plating during Extreme Fast Charging. *Cell Rep. Phys. Sci.* **2020,** *1*, 100114.
12. Tanim, T. R.; Dufek, E. J.; Dickerson, C. C.; Wood, S. M., Electrochemical Quantification of Lithium Plating: Challenges and Considerations. *J. Electrochem. Soc.* **2019,** *166*, A2689-A2696.
13. Burns, J. C.; Stevens, D. A.; Dahn, J. R., *In-Situ* Detection of Lithium Plating Using High Precision Coulometry. *J. Electrochem. Soc.* **2015,** *162*, A959-A964.
14. Yan, K.; Lu, Z.; Lee, H.-W.; Xiong, F.; Hsu, P.-C.; Li, Y.; Zhao, J.; Chu, S.; Cui, Y., Selective Deposition and Stable Encapsulation of Lithium Through Heterogeneous Seeded Growth. *Nat. Energy* **2016,** *1*, 16010.
15. Jin, S.; Ye, Y.; Niu, Y.; Xu, Y.; Jin, H.; Wang, J.; Sun, Z.; Cao, A.; Wu, X.; Luo, Y.; Ji, H.; Wan, L. J., Solid-Solution-Based Metal Alloy Phase for Highly Reversible Lithium Metal Anode. *J. Am. Chem. Soc.* **2020,** *142*, 8818-8826.

16.     Liu, F.; Xu, R.; Wu, Y.; Boyle, D. T.; Yang, A.; Xu, J.; Zhu, Y.; Ye, Y.; Yu, Z.; Zhang, Z.; Xiao, X.; Huang, W.; Wang, H.; Chen, H.; Cui, Y., Dynamic Spatial Progression of Isolated Lithium During Battery Operations. *Nature* **2021,** *600*, 659-663.

17.     Chen, Y.; Chen, K.-H.; Sanchez, A. J.; Kazyak, E.; Goel, V.; Gorlin, Y.; Christensen, J.; Thornton, K.; Dasgupta, N. P., Operando Video Microscopy of Li Plating and Re-Intercalation on Graphite Anodes During Fast Charging. *J. Mater. Chem. A* **2021,** *9*, 23522-23536.

18.     Gao, T.; Han, Y.; Fraggedakis, D.; Das, S.; Zhou, T.; Yeh, C.-N.; Xu, S.; Chueh, W. C.; Li, J.; Bazant, M. Z., Interplay of Lithium Intercalation and Plating on a Single Graphite Particle. *Joule* **2021,** *5*, 393-414.

19.     Wandt, J.; Jakes, P.; Granwehr, J.; Eichel, R.-A.; Gasteiger, H. A., Quantitative and Time-Resolved Detection of Lithium Plating on Graphite Anodes in Lithium Ion Batteries. *Mater. Today* **2018,** *21*, 231-240.

20.     Aurbach, D.; Zinigrad, E.; Cohen, Y.; Teller, H., A Short Review of Failure Mechanisms of Lithium Metal and Lithiated Graphite Anodes in Liquid Electrolyte Solutions. *Solid State Ionics* **2002,** *148*, 405-416.

21.     Gachot, G.; Grugeon, S.; Eshetu, G. G.; Mathiron, D.; Ribière, P.; Armand, M.; Laruelle, S., Thermal Behaviour of the Lithiated-Graphite/Electrolyte Interface Through GC/MS Analysis. *Electrochim. Acta* **2012,** *83*, 402-409.

22.     Dong, K.; Xu, Y.; Tan, J.; Osenberg, M.; Sun, F.; Kochovski, Z.; Pham, D. T.; Mei, S.; Hilger, A.; Ryan, E.; Lu, Y.; Banhart, J.; Manke, I., Unravelling the Mechanism of Lithium Nucleation and Growth and the Interaction with the Solid Electrolyte Interface. *ACS Energy Lett.* **2021,** *6*, 1719-1728.

23.     Qian, J.; Wang, S.; Li, Y.; Zhang, M.; Wang, F.; Zhao, Y.; Sun, Q.; Li, L.; Wu, F.; Chen, R., Lithium Induced Nano-Sized Copper with Exposed Lithiophilic Surfaces to Achieve Dense Lithium Deposition for Lithium Metal Anode. *Adv. Funct. Mater.* **2020,** *31*, 2006950.

24.     Thirumalraj, B.; Hagos, T. T.; Huang, C.-J.; Teshager, M. A.; Cheng, J.-H.; Su, W.-N.; Hwang, B.-J., Nucleation and Growth Mechanism of Lithium Metal Electroplating. *J. Am. Chem. Soc.* **2019,** *141*, 18612-18623.

25.     Yin, X.; Tang, W.; Jung, I. D.; Phua, K. C.; Adams, S.; Lee, S. W.; Zheng, G. W., Insights into Morphological Evolution and Cycling Behaviour of Lithium Metal Anode Under Mechanical Pressure. *Nano Energy* **2018,** *50*, 659-664.

26.     Fang, C.; Lu, B.; Pawar, G.; Zhang, M.; Cheng, D.; Chen, S.; Ceja, M.; Doux, J.-M.; Musrock, H.; Cai, M.; Liaw, B.; Meng, Y. S., Pressure-Tailored Lithium Deposition and Dissolution in Lithium Metal Batteries. *Nat. Energy* **2021,** *6*, 987-994.

27.     Pelton, A. D., The Ag−Li (Silver-Lithium) System. *Bull. Alloy Phase Diagr.* **1986,** *7*, 223-228.

28.     Zhang, S.; Yang, G.; Liu, Z.; Weng, S.; Li, X.; Wang, X.; Gao, Y.; Wang, Z.; Chen, L., Phase Diagram Determined Lithium Plating/Stripping Behaviors on Lithiophilic Substrates. *ACS Energy Lett.* **2021,** *6*, 4118-4126.

29.     Dębski, A.; Terlicka, S.; Budziak, A.; Gąsior, W., Calorimetric and XRD Studies of Ag-Rich Alloys from Ag-Li System. *J. Alloys Compd.* **2018,** *732*, 210-217.

30.     Taillades, G.; Sarradin, J., Silver: High Performance Anode for Thin Film Lithium Ion Batteries. *J. Power Sources* **2004,** *125*, 199-205.

31.     Ho, A. S.; Parkinson, D. Y.; Finegan, D. P.; Trask, S. E.; Jansen, A. N.; Tong, W.; Balsara, N. P., 3D Detection of Lithiation and Lithium Plating in Graphite Anodes during Fast Charging. *ACS Nano* **2021,** *15*, 10480-10487.

32.     Kong, L.-L.; Wang, L.; Ni, Z.-C.; Liu, S.; Li, G.-R.; Gao, X.-P., Lithium–Magnesium Alloy as a Stable Anode for Lithium–Sulfur Battery. *Adv. Funct. Mater.* **2019,** *29*, 1808756.

33.    Krauskopf, T.;  Mogwitz, B.;  Rosenbach, C.;  Zeier, W. G.; Janek, J., Diffusion Limitation of Lithium Metal and Li–Mg Alloy Anodes on LLZO Type Solid Electrolytes as a Function of Temperature and Pressure. *Adv. Energy Mater.* **2019,** *9*, 1902568.

34.    Ilavsky, J., Nika: Software for Two-Dimensional Data Reduction. *J. Appl. Crystallogr.* **2012,** *45*, 324-328.
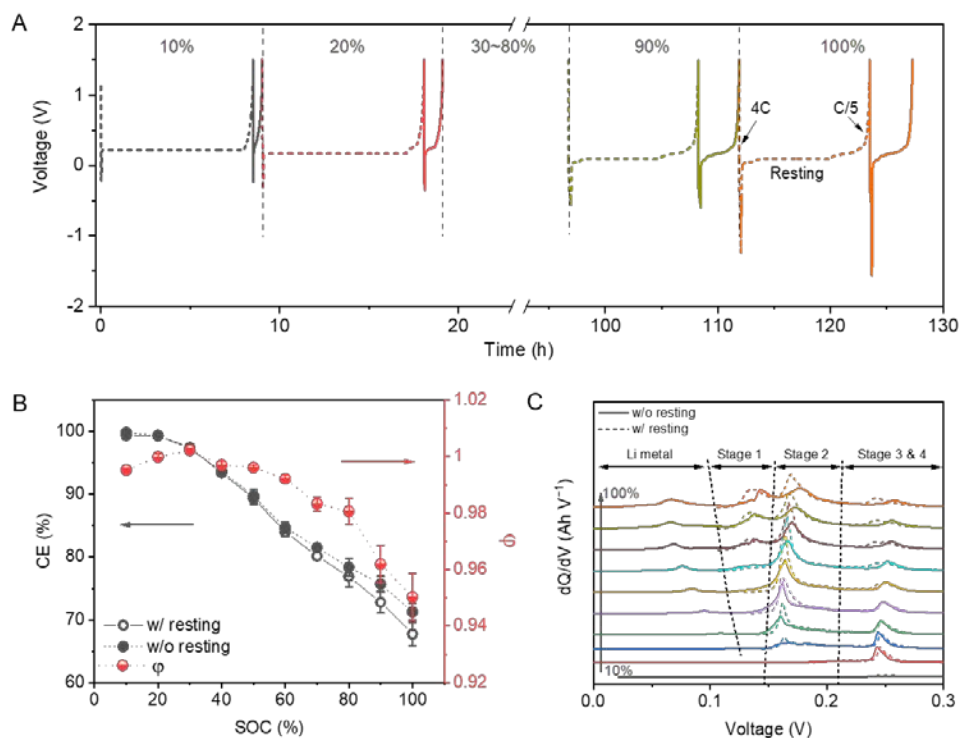
**Figure 1.** (A) Representative voltage profiles of a Gr/Li cell charged at 4C to different SOCs from 10% to 100% and then discharged at C/5, at each SOC, the cell is first cycled with resting and then cycled without resting after charge; (B) CE of Gr/Li half-cells cycled to different SOCs with and without resting after 4C charge and the corresponding $CE_{w/ \, resting}/CE_{w/o \, resting}$ (denoted as φ) value, error bar shows the standard deviation calculated from triplicate cells; (C) $dQ/dV$ curves during discharge after 4C charge to different SOCs. Cells are discharged to 1.5 V at C/5.
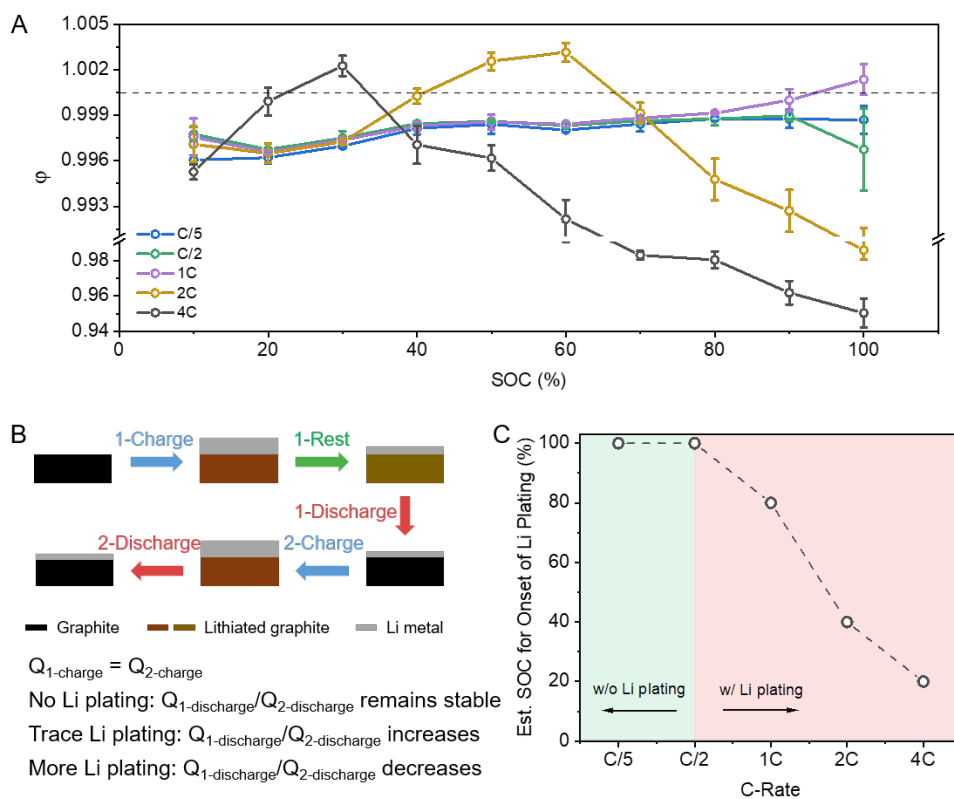
**Figure 2.** (A) $CE_{w/\ resting}/CE_{w/o\ resting}$ (denoted as $\varphi$) values at various SOCs for Gr/Li half-cells charged at different rates, error bar shows the standard deviation calculated from triplicate cells; (B) schematics shows the charge-discharge processes for graphite with and without resting after fast charge; (C) estimated SOCs for the onsets of Li plating at different rates. Cells are discharged to 1.5 V at C/5.
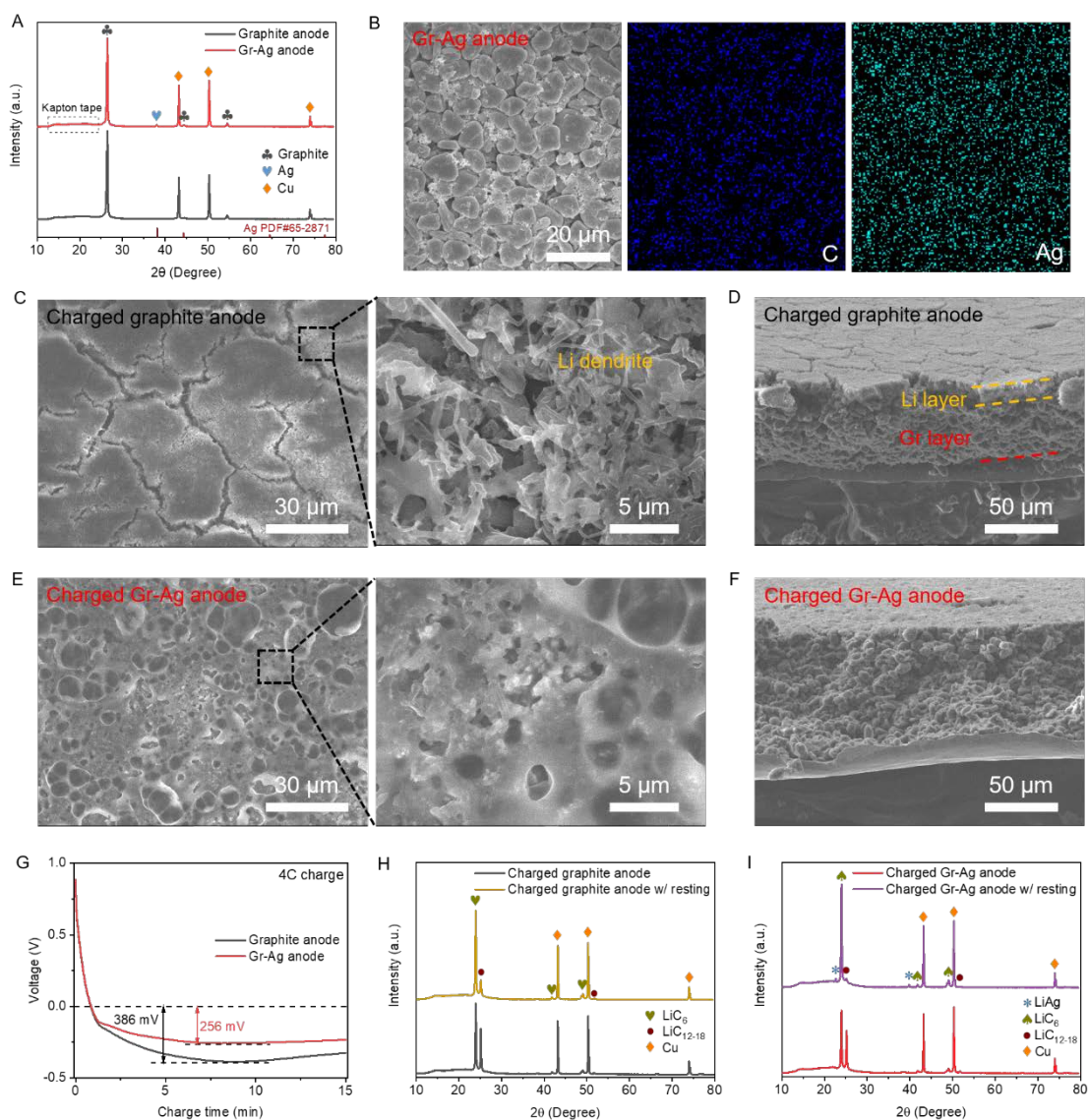
**Figure 3.** (A) XRD patterns of graphite and Gr-Ag electrodes; (B) SEM image and EDS mapping of Gr-Ag electrode; (C) top-view and (D) cross-section SEM images of graphite electrode after 4C fast charge to 100% SOC; (E) top-view and (F) cross-section SEM images of Gr-Ag electrode after 4C fast charge to 100% SOC; (G) 4C charge profiles of Gr and Gr-Ag electrodes to 100% SOC; and XRD patterns of (H) graphite and (I) Gr-Ag electrodes after 4C charge to 100% SOC with and without resting. The XRD patterns are normalized to the Cu peaks from current collector.
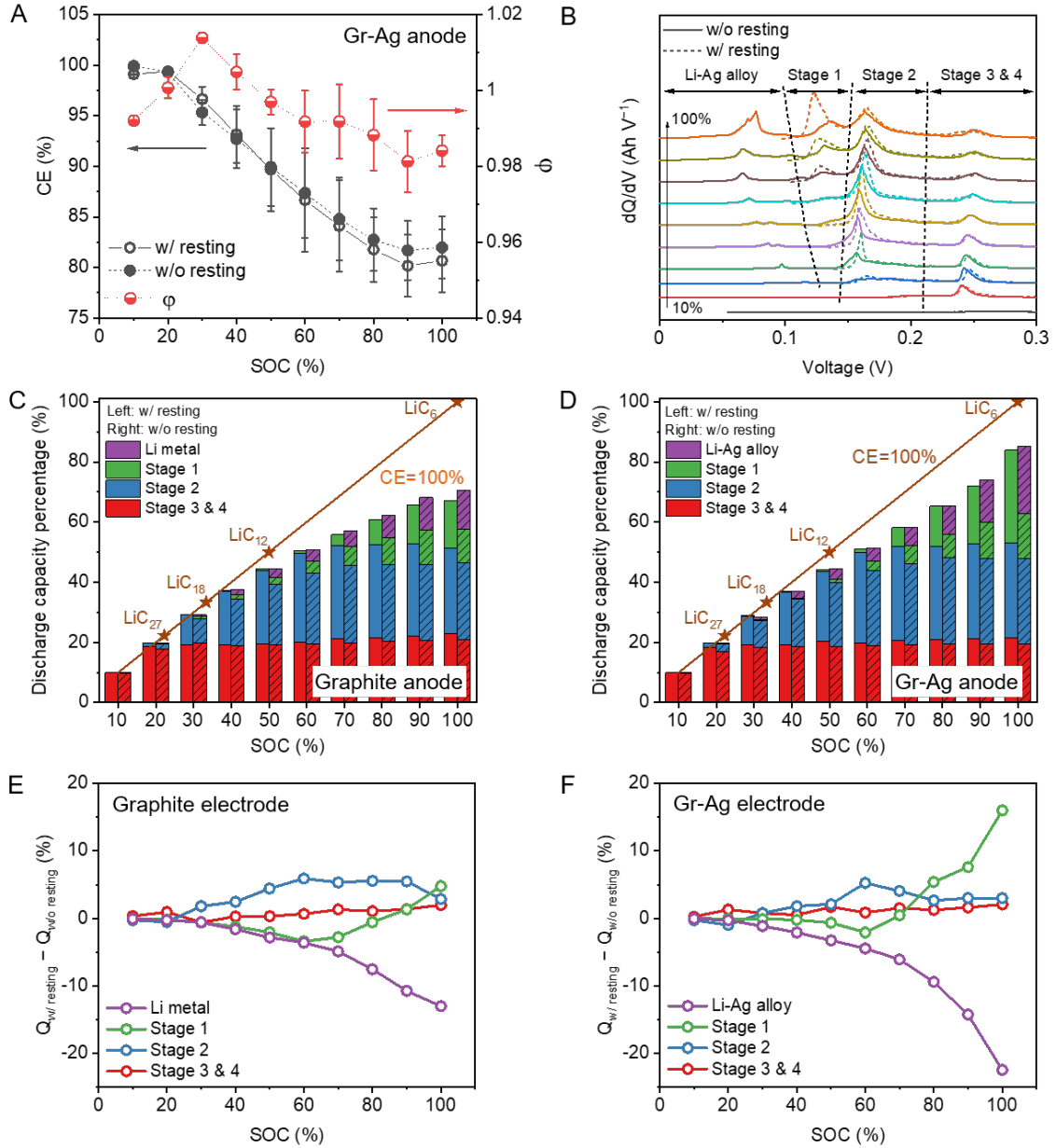
**Figure 4.** (A) CE and $CE_{w/\ resting}/CE_{w/o\ resting}$ (denoted as φ) value of Gr-Ag electrode in Li half-cells, error bar shows the standard deviation calculated from triplicate cells; (B) $d$Q/$d$V plots during discharge after 4C charge to different SOCs; normalized discharge capacities of different phases for fast-charged (C) graphite and (D) Gr-Ag electrodes at different SOCs; and the difference in normalized discharge capacity with and without resting after fast charge of (E) graphite and (F) Gr-Ag electrodes. Cells are discharged to 1.5 V at C/5.
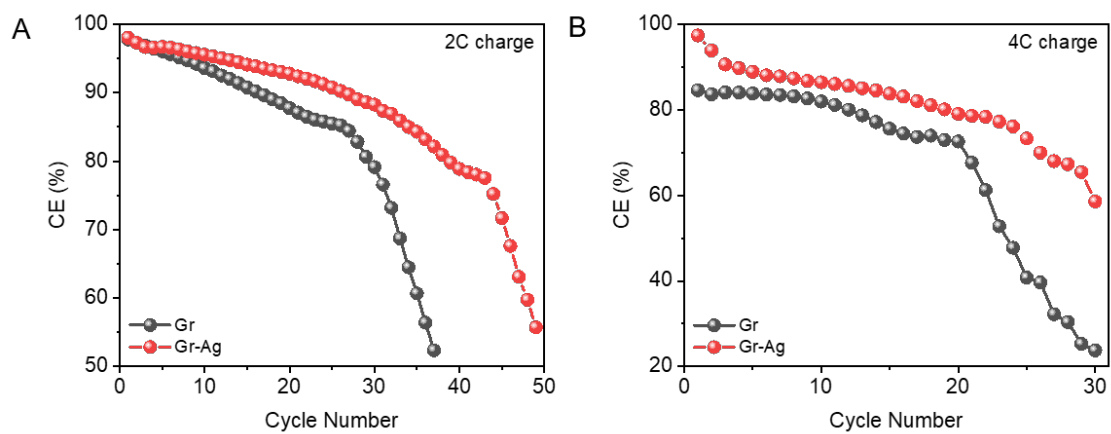
**Figure 5.** CE of graphite and Gr-Ag electrodes in Li half-cells when charged to 100% SOC at (A) 2C and (B) 4C. Cells are discharged to 1.5 V at C/5.

# TOC Graphic
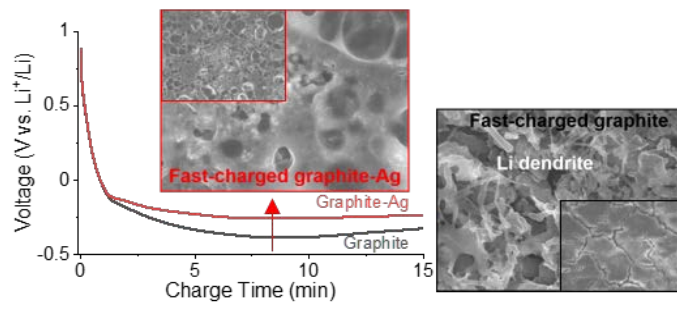
**Supporting Information for**

**Insights into the Enhanced Reversibility of Graphite Anode upon Fast Charging Through Li Reservoir**

Ji Qian, Tianyu Zhu, Di Huang, Gao Liu, Wei Tong*

*Energy Storage and Distributed Resources Division, Lawrence Berkeley National Laboratory, Berkeley, California 94720, United States*

Email: weitong@lbl.gov
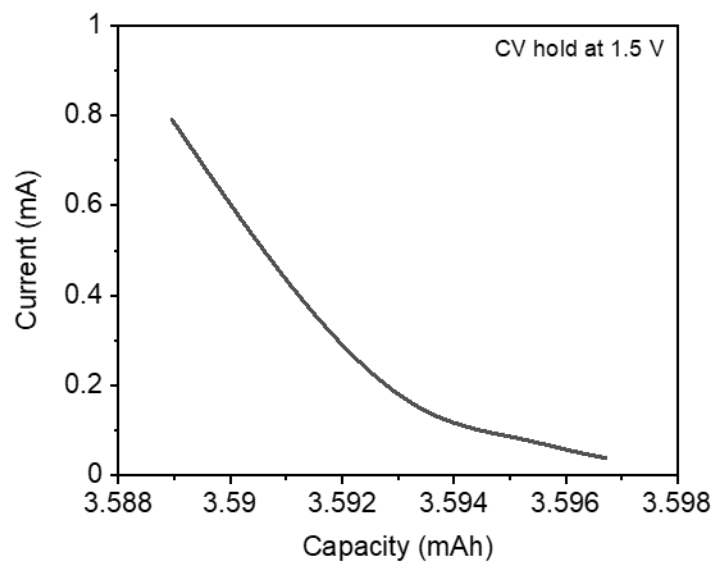
**Figure S1**. Current profile of Gr/Li cell during the constant voltage (CV) hold at 1.5 V after C/5 discharge (5% initial current). Prior to CV hold, the cell is initially charged to 100% SOC at 4C and then discharged to 1.5 V.
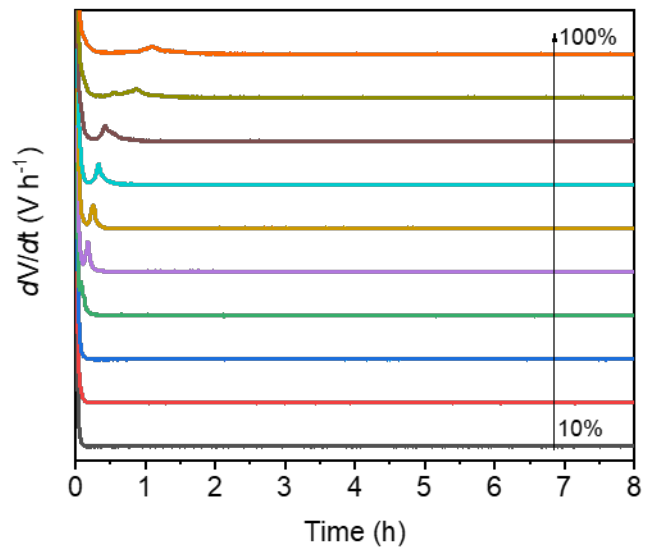
**Figure S2**. Differential voltage profiles of the Gr/Li cells at various SOCs during resting after 4C charge.
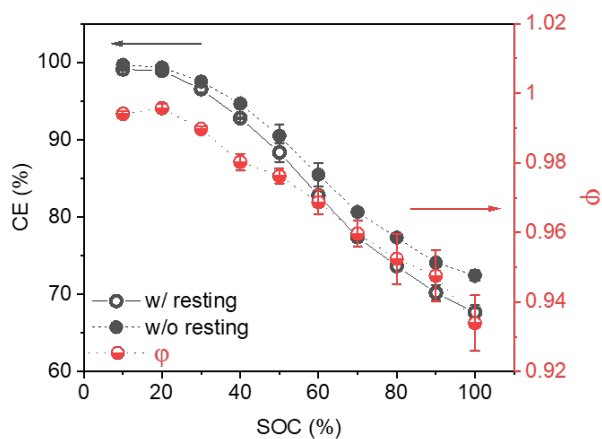
**Figure S3.** CE of Gr/Li half-cells cycled to different SOCs with and without resting after 4C charge and the corresponding $CE_{w/\,resting}/CE_{w/o\,resting}$ (denoted as φ) value, error bar shows the standard deviation calculated from triplicate cells. Cells are charged at 4C and then discharged to 1.5 V at C/5. For the two cycles at each SOC, a resting process is applied in the latter cycle.
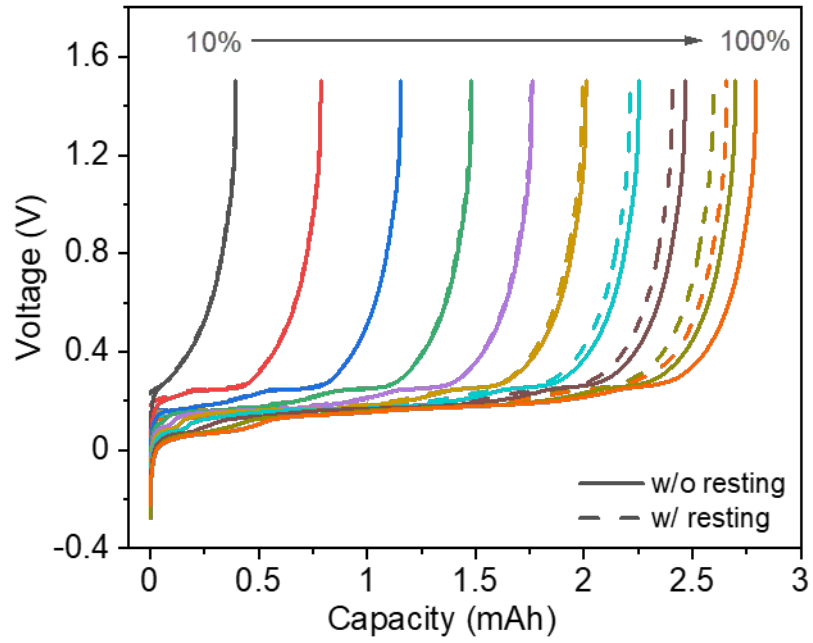
**Figure S4.** Discharge profiles of Gr/Li cells after 4C charge to different SOCs. The cell is discharged to 1.5 V at C/5.
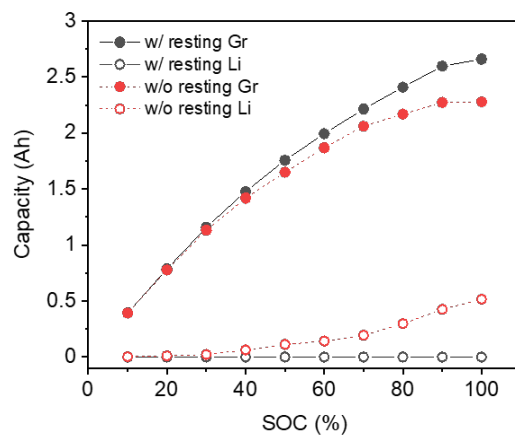
**Figure S5.** Specific discharge capacity from graphite and plated Li after 4C charge with and without resting. The capacity is calculated by integrating the areas corresponding to lithiated graphite phases and plated Li.
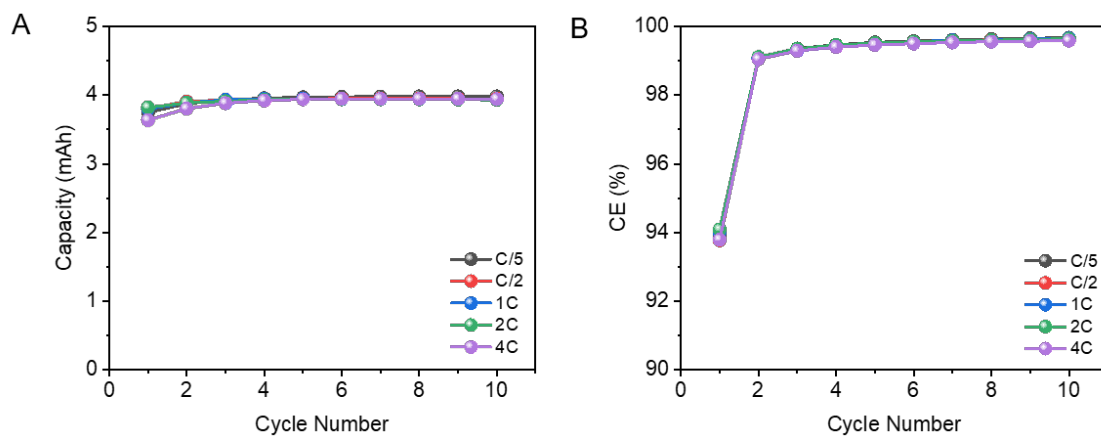
**Figure S6.** (A) Discharge capacity and (B) CE of Gr/Li cell during formation cycles for different charge rate studies. The cells are cycled between 1.5 and 0.01 V at C/10, 1C capacity is 330 mAh g$^{-1}$.
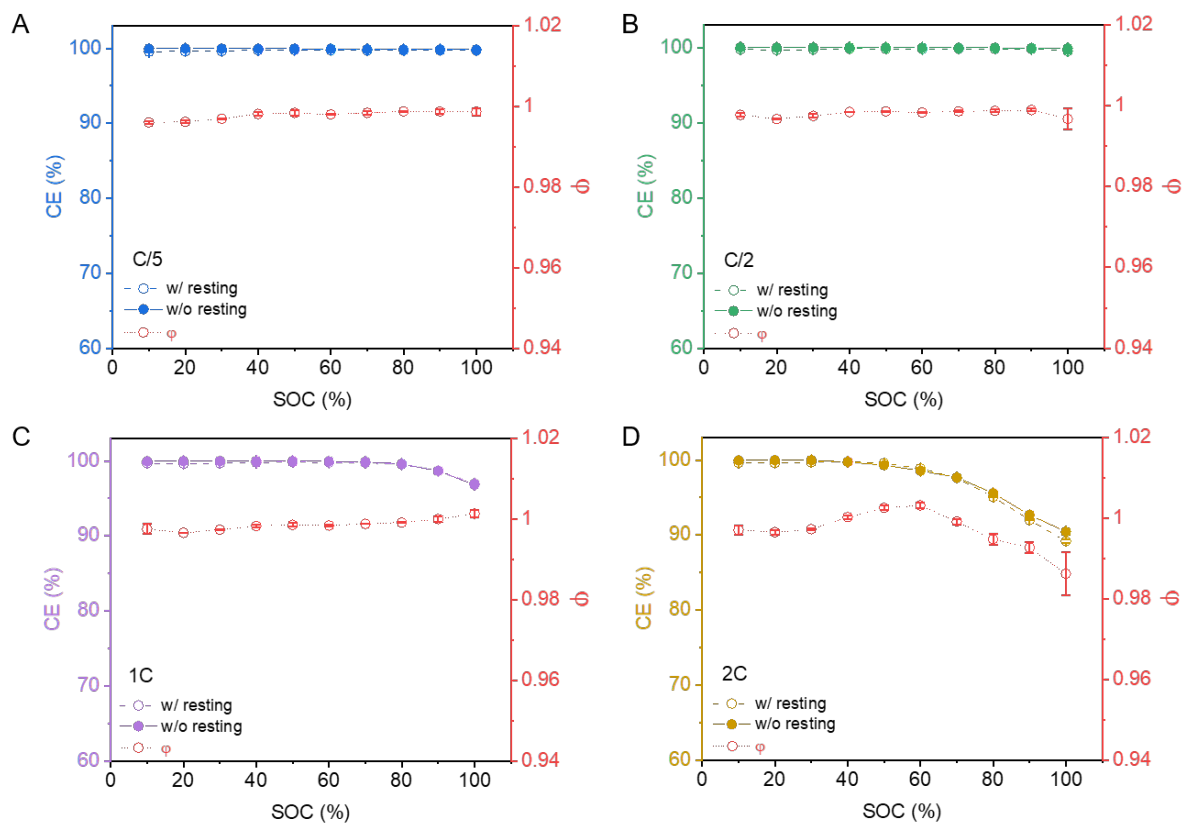
**Figure S7.** CE of Gr/Li cell charged to different SOCs at a rate of (A) C/5, (B) C/2, (C) 1C and (D) 2C and corresponding CE$_{w/\ resting}$/CE$_{w/o\ resting}$ (denoted as φ) value, error bar shows the standard deviation calculated from triplicate cells. Cells are charged to certain SOCs (from 10% to 100% progressively) and then discharged to 1.5 V at C/5. For the two cycles at each SOC, a resting process is applied in the former cycle.
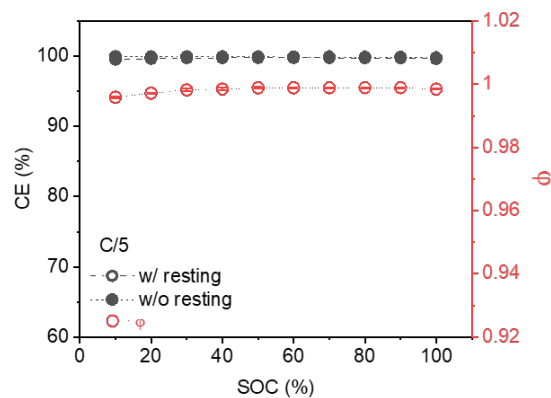
**Figure S8.** CE of Gr/Li cell charged to different SOCs at C/5 and corresponding $CE_{w/\ resting}/CE_{w/o\ resting}$ (denoted as φ) value, error bar shows the standard deviation calculated from triplicate cells. Cells are charged to certain SOCs (from 10% to 100% progressively) and then discharged to 1.5 V at C/5. For the two cycles at each SOC, a resting process is applied in the latter cycle to understand the influence of resting process on CE when there is no Li deposition at low charging rate.
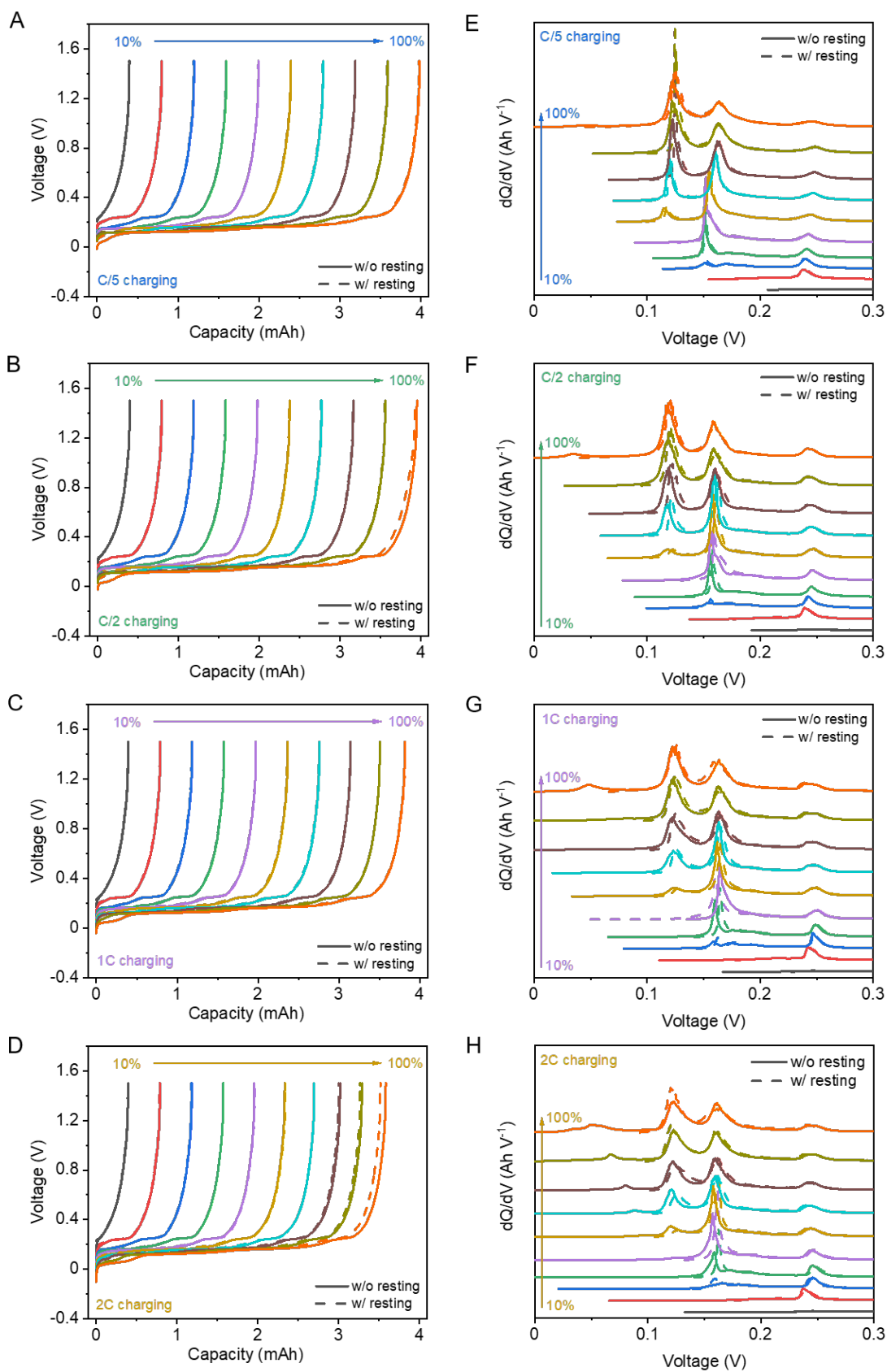
**Figure S9.** (A-D) Discharging profiles and (E-H) $dQ/dV$ plots of Gr/Li cells after charge at different rates with and without resting. The charge rates are C/5, C/2, 1C, and 2C and discharge rate is C/5.
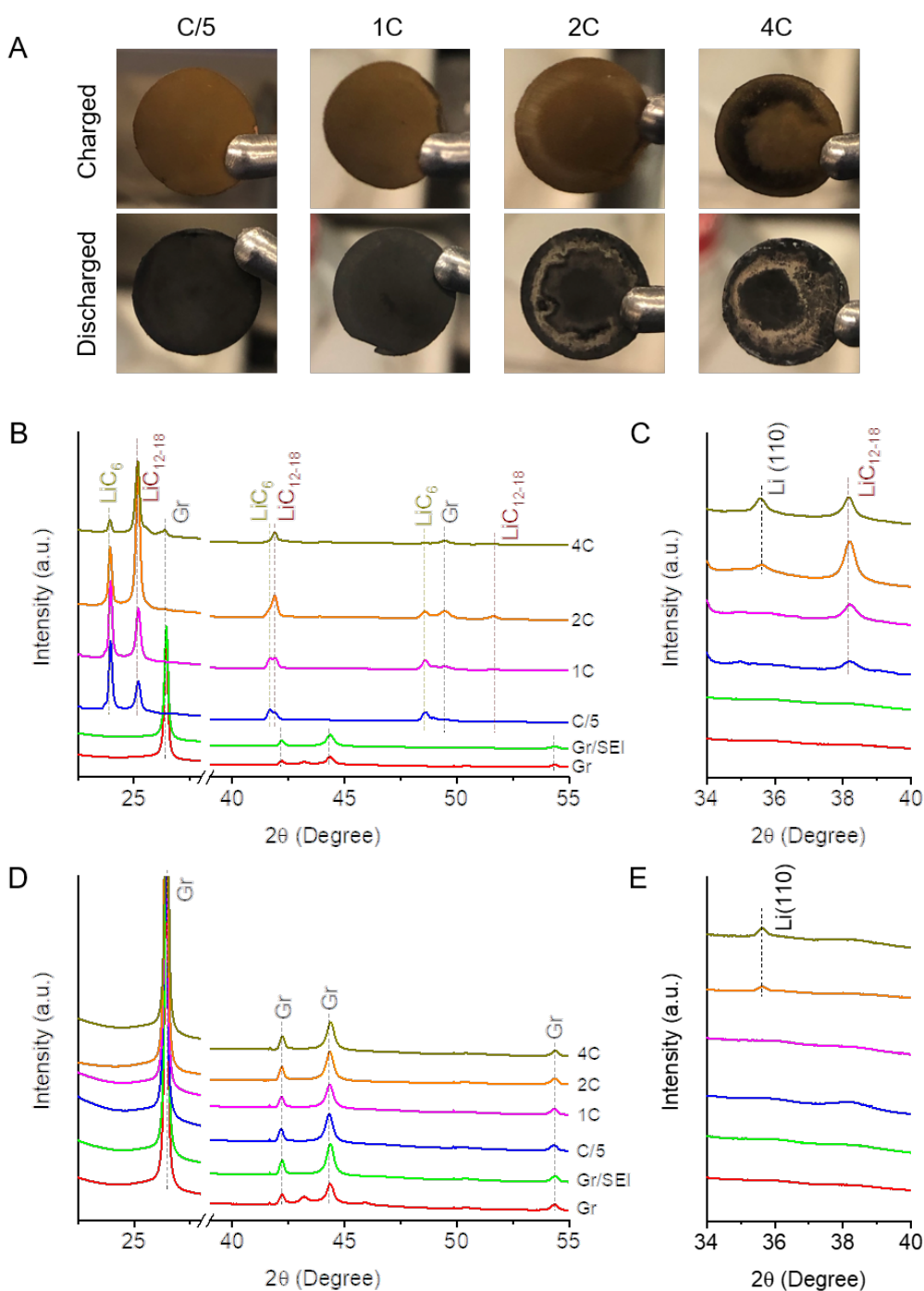
**Figure S10.** (A) Photographs of the graphite electrodes charged to 100% SOC at different rates and then discharged to 1.5 V at C/5; and WAXS patterns collected after (B, C) charge at various rates, followed by (D, E) discharge at C/10 along with graphite electrodes at pristine state and after three formation cycles with SEI (Gr/SEI). All cells are cycled between 1.5 and 0.01 V with three formation cycles at C/10 (1C = 330 mAh g$^{-1}$) and the capacity at the 4$^{th}$ cycle for charge rate study is based on the discharge capacity during the formation cycle for accurate SOC. Graphite electrodes are scraped from the Cu current collectors for WAXS measurements to remove strong Cu signals.
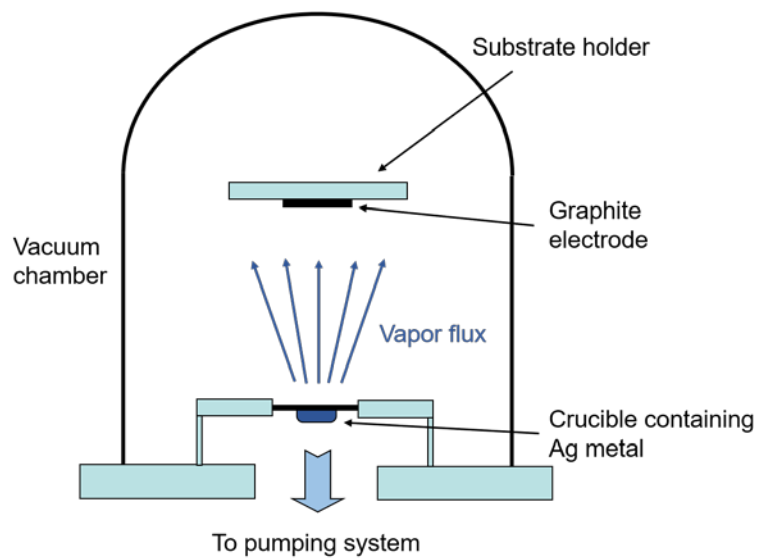
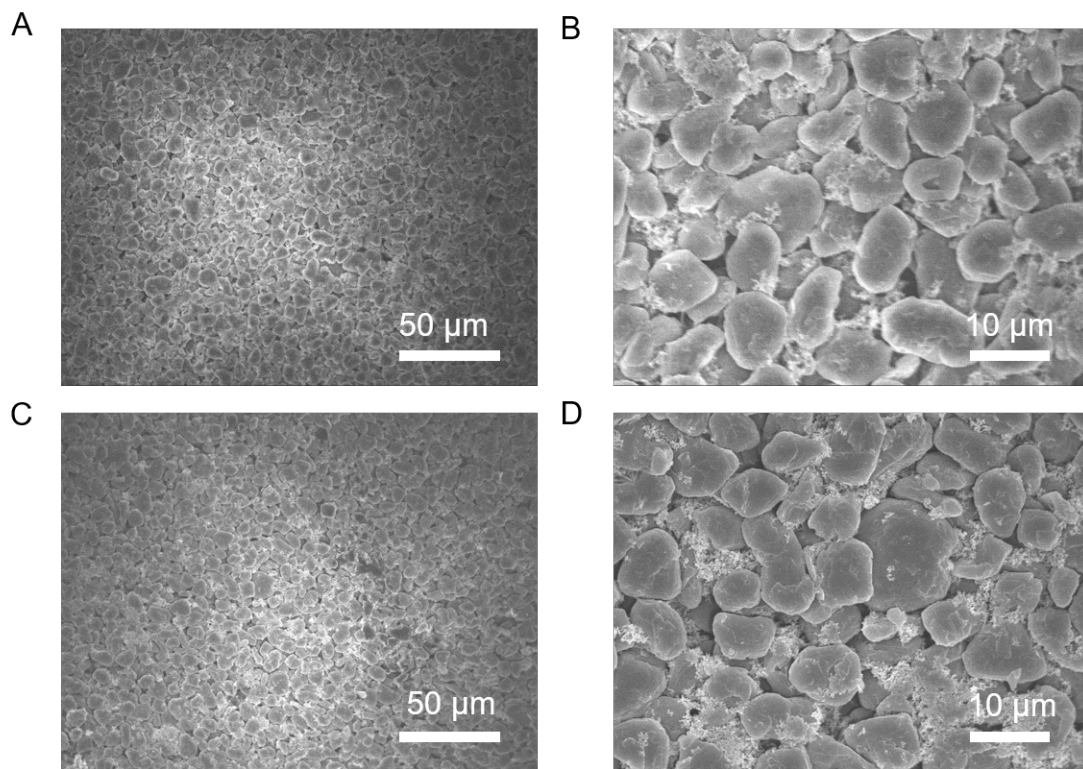**Figure S11.** Schematic of Ag coated graphite electrode processing via thermal deposition method.

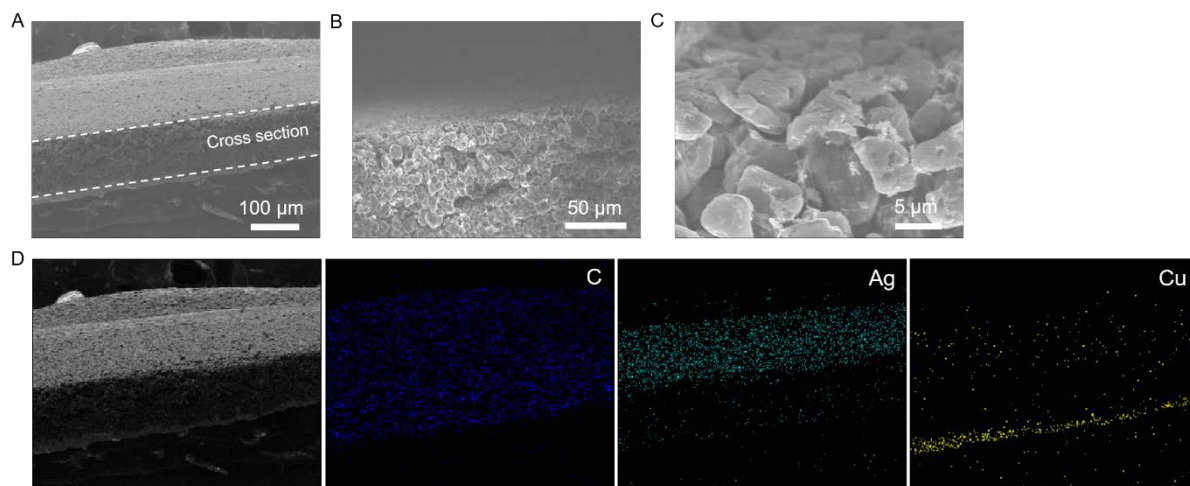**Figure S12.** Top-view SEM images of (A, B) graphite and (C, D) Gr-Ag electrodes.

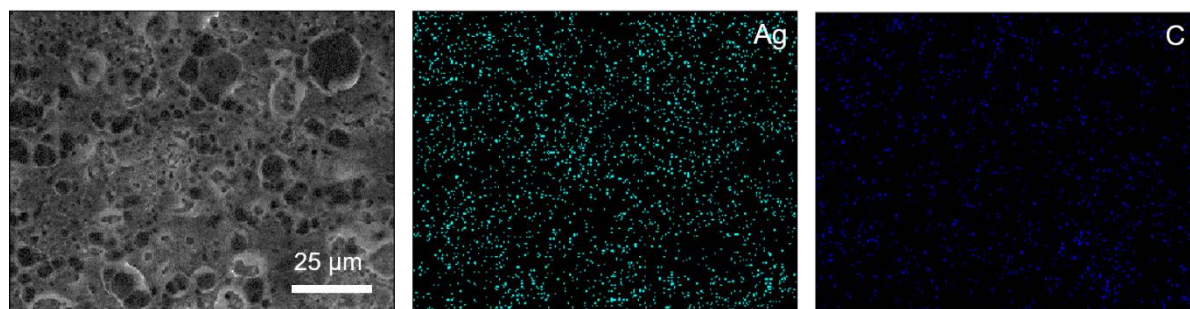**Figure S13.** (A-C) Cross-section SEM images and (D) EDS elemental mapping of Gr-Ag electrode.

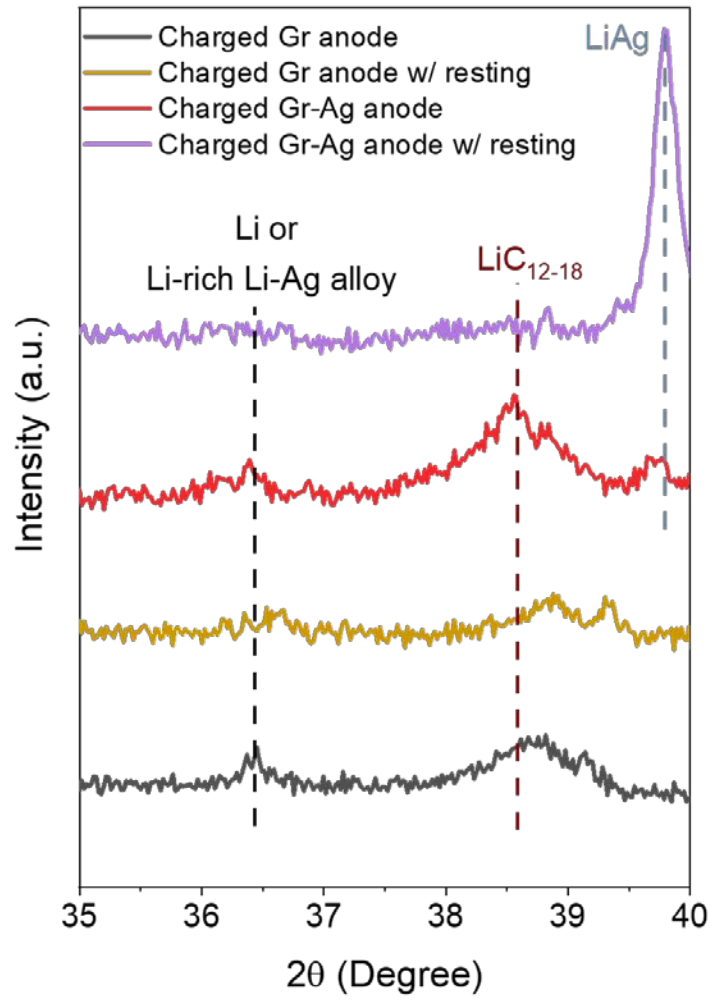**Figure S14.** EDS maps of Gr-Ag electrode after 4C charge from the top view.

**Figure S15.** XRD patterns of graphite and Gr-Ag electrodes after 4C charge to 100% SOC with and without resting.

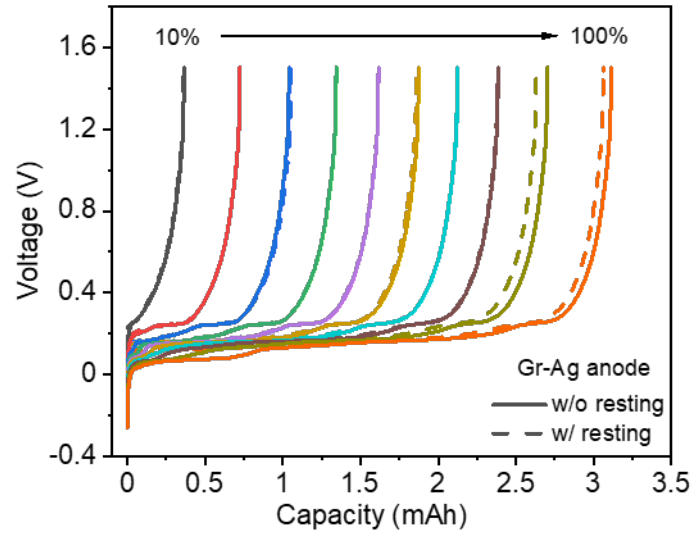**Figure S16.** Discharge profiles of Gr-Ag/Li cells after 4C charge to different SOCs with and without resting. Cells are discharged to 1.5 V at C/5.